RSC Advances

PAPER

View Article Online
View Journal | View Issue

Cite this: *RSC Adv.*, 2026, **16**, 22352

Synthesis, structural characterization and molecular docking analysis of novel β-ketoiminato palladium(II) complexes with anticancer properties

Deeb Taher, *[a] Belal Khalil,[a] Sara AlNaimat,[a] Morad Mustafa,[bc] Zakariyya Ishtaiwi,[d] Wissam Helal,[a] Marcus Korb,[e] Tuqa Abu Thiab,[f] Amer Imraish,[f] Tareq Alhindi,[f] Ahmad Makahleh,[a] Mohammad W. Amer[a] and Duha H. Abdelrahman[a]

A novel series of palladium(II) coordination complexes of the formula $[Pd(CH_3C(NAr)CHC(O)CH_3)_2]$ (**4a–j**) were synthesized by the reaction of enaminone ligands (**3a–j**) with $[PdCl_2(NCCH_3)_2]$ in a molar ratio of 2 : 1 in the presence of ^{t}BuOK. The square planar coordination geometry around Pd(II) of the **4c** complex, with electrostatic potential calculations rationalizing the formation of C–H···π contacts, leading to chain structures, was confirmed by single-crystal X-ray diffraction. UV-vis spectra, supported by TD-DFT (B3LYP) calculations, indicated that the long-wavelength absorptions arose from intra-ligand charge transfer transitions (π → π*) involving HOMO–LUMO+1 excitations, with Pd(II) orbitals contributing to the HOMO. Thermogravimetric analysis demonstrated high thermal stability of the series. Biological evaluation revealed notable cytotoxicities of the compounds **4b**, **4d**, **4h**, **4i**, and **4j**. The compound **4i** shows the strongest activity (IC_{50} = 5.42 μM, MCF-7; 17.20 μM, and HCT-116) and high selectivity toward cancer cells. Molecular docking against oncogenic targets (PIK3CA-E545K, ERBB4-Y1242C, KRAS-G13D, PIK3CA-H1047R, and ATM-A112V) identified *meta*- and *para*-substituted analogues (**4b**, **4c**, and **4h**) as the most favorable binders, while bulky *ortho* substituents reduced the affinity due to steric effects. Docking against PIK3CA-E545K produced binding energies that qualitatively paralleled several of the measured MCF-7 selectivity indices, with planar aromatic interactions and hydrophobic contacts defining the structure–activity relationships.

Received 2nd December 2025
Accepted 2nd April 2026

DOI: 10.1039/d5ra09325b

rsc.li/rsc-advances

1. Introduction

Schiff base compounds are considered a well-established class of organic compounds, valued for their straightforward synthesis through the reaction of primary aromatic amines with carbonyl compounds.[1–3] Their role as ligands in coordination chemistry, combined with their high stability and broad range of biological activities, makes them significant in various scientific applications. Researchers today are particularly focusing on the pharmacological potential of this class of compounds and their metal complexes, exploring their antitumoral, antiviral, antibacterial, antifungal, and antioxidant properties.[4–8] Schiff base ligands are pivotal in the design of coordination complexes, especially with relevant transition metals, such as Pd^{2+}, Pt^{2+}, Co^{2+}, Ni^{2+}, Cu^{2+}, and Zn^{2+}.[9–14] In addition to enhanced biological activity, these complexes acquire a lipophilic nature, improving their ability to traverse biological membranes. Structural modifications, such as aromatic substitutions with halogen, hydroxyl, or methoxy groups, have shown further enhancement of their antifungal, antibacterial, antitumoral, and antioxidant properties.[5,15–20] A major challenge in modern pharmaceutical research is the development of therapeutic agents that operate through novel mechanisms of action while exhibiting minimal side effects, mainly for the treatment of cancer and infection.[21,22] Coordination chemistry has emerged as a promising approach to address this demand due to its extensive research, diverse biological activities, and low toxicity.[23,24] Among coordination chemists, Schiff base-derived palladium complexes have attracted significant interest due to their diverse biological properties.[25] A wide range of palladium(II) coordination complexes has been reported, many of which demonstrate significant cytotoxic activity against a wide spectrum of cancer

[a]*Chemistry Department, The University of Jordan, Amman, 11942, Jordan. E-mail: d.taher@ju.edu.jo*

[b]*Department of Pharmacy, College of Pharmacy, Al-Zaytoonah University, PO Box: 130, Amman 11733, Jordan*

[c]*Chemistry Program, Science Division, New York University Abu Dhabi, P.O. Box: 129188, Abu Dhabi, United Arab Emirates*

[d]*Department of Chemistry, Faculty of Science, Al-Balqa Applied University, Al Salt 19117, Jordan*

[e]*School of Molecular Sciences, The University of Western Australia, 35 Stirling Highway, Crawley, Perth, Western Australia 6009, Australia*

[f]*Department of Biological Sciences, The University of Jordan, Amman, 11942, Jordan*

cell lines.[26–30] These complexes exhibit antimicrobial,[31,32] antifungal,[33] and anticancer activities,[34–36] along with other biochemical and pharmacological properties. Palladium(II) complexes have garnered considerable interest in bioinorganic chemistry largely owing to their structural similarity to platinum(II) compounds, with both ions exhibiting comparable coordination geometries and ionic radii.[37,38] Compared with Pt(II) analogues, Pd(II) complexes typically exhibit higher thermodynamic and kinetic lability, which are characterized by ligand exchange rates that are approximately 10^4 to 10^5 times faster.[38,39] This high reactivity can lead to premature hydrolysis before reaching the pharmacological target; moreover, the use of chelating ligands has helped stabilize Pd(II) complexes,[38] making them more kinetically inert.[40,41] Additionally, palladium complexes offer superior solubility compared with platinum-based compounds,[42] increasing their attractiveness for biomedical applications. Although platinum-based drugs (*i.e.*, carboplatin, cisplatin, and oxaliplatin) remain the cornerstone agents in cancer therapy, their clinical utility is frequently constrained by severe side effects.[43] Palladium complexes, with their improved stability and selectivity, present a promising alternative with their potential therapeutic advantages.[38,39] Furthermore, β-ketoiminate ligands, commonly referred to as "NAcAc", have expanded the possibilities for modifying the behavior of transition metal complexes. The ability to fine-tune steric and electronic properties through ligand substitutions allows for greater control over the resulting metal complexes.[44–46] The versatility and tunable properties of NAcAc complexes render them promising candidates for applications in cancer therapy and antimicrobial treatment strategies.

McGowan *et al.* reported iridium and ruthenium complexes with naphthoquinone (*O*,*O*), β-ketoiminato (*N*,*O*), and picolinamide (*N*,*N*) ligands to investigate the role of coordination mode in cytotoxicity.[47] The activity correlated with the ligand binding mode, following the order of (*N*,*O*) > (*O*,*O*) > (*N*,*N*). An expanded complex library incorporating functionalized β-ketoiminate ligands exhibited cytotoxicity against multiple human cancer types, such as breast, colorectal, and human ovarian (including cisplatin-resistant) carcinomas.[48,49] Carbonyl complexes based on bis(β-ketoiminato) ruthenium(II) were synthesized but showed lower activity, which was attributed to aqueous instability.[50] Mechanistic studies indicated that (*N*,*N*) complexes hydrolyzed quickly and bound guanine differently, whereas (*N*,*O*) complexes hydrolyzed more slowly, reducing cytotoxicity.[51,52]

Recently, we reported on palladium complexes incorporating functionalized β-ketoiminate ligands for significant effectiveness against human breast carcinoma.[53,54] Molecular docking studies were performed to evaluate the interactions of these Pd(II) complexes with the target proteins PIK3CA-E545K, ERBB4-Y1242C, and BRAF-V600E, revealing moderate-to-strong binding affinities.[12,53] Docking results demonstrated that bulky substituents on Pd(II) complexes reduce optimum binding interactions by preventing them from being accommodated within the protein binding sites due to steric hindrance.[53,54] Interestingly, it was discovered that the biological activity of Pd(II) complexes was significantly affected by the location of the substituents on the NAcAc ligand.[47–50] Based on these findings, the present study focuses on the design of palladium(II) coordination complexes with β-ketoiminate ligands bearing reduced steric bulk and evaluates their cytotoxic potential against tumor cell lines.

As part of our ongoing research into palladium compounds,[12,53–62] this study presents the synthesis, spectral analysis, theoretical investigations and X-ray crystallography of Pd(II) complexes containing Schiff bases. Characterization was achieved using UV-vis, IR, and NMR spectroscopy, as well as elemental and thermal analyses. The crystal structure of complex **4c** was determined, confirming its geometry. Further investigations, including Hirshfeld surface analysis, density functional theory (DFT) calculations, and time-dependent DFT (TD-DFT) analysis, provided insights into the crystallographic interactions, electronic properties, and UV-vis spectral transitions. These complexes were evaluated for *in vitro* antitumor activity against various human cell lines (MCF-7 and HT-29) alongside docking studies. Cancer cell lines were obtained from the ATCC (Manassas, VA), MCF7 human breast cancer cell line (ATCC® HTB-22™, USA), HCT-116 colon cancer cell line (ATCC CCL-247™, USA) and human skin fibroblast (ATCC® PCS-201-012™).

2. Results and discussion

2.1. Synthesis

Scheme 1 depicts the synthetic routes used to synthesize ligands[63–72] and their corresponding complexes.[73,74] Moderate to excellent yields (55–92%) of the complexes were achieved. The obtained Pd(II) complexes exhibit good solubility in some common solvents, such as tetrahydrofuran, acetonitrile, chloroform, dichloromethane, and dimethyl sulfoxide. The complexes are non-hygroscopic and visually air-stable in both

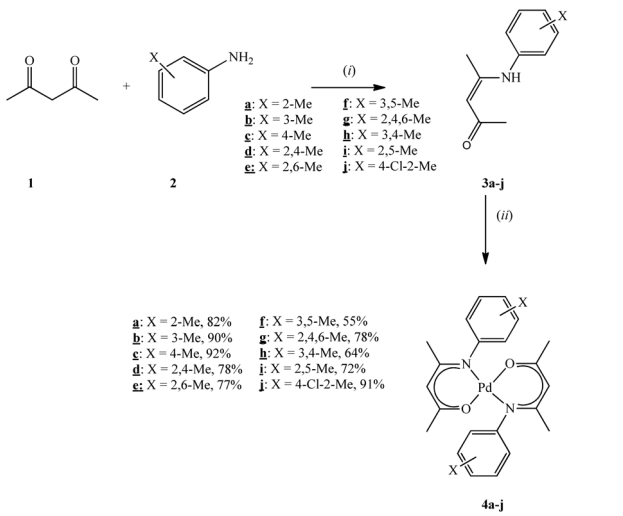

Scheme 1 Synthesis of **4a–j**. (i) **2a–j** (1 equiv.), substituted aniline (1 equiv.), refluxing toluene, and 24 h. (ii) **3a–j** (2 equiv.), KO^tBu (2 equiv.), $[PdCl_2(NCCH_3)_2]$ (1 equiv.), methanol, ambient temperature, and 3 d. Yields are based on **3a–j**.

the solid-state and solution for several months. Interestingly, it was discovered that the melting points of the complexes is higher than those of the ligands. This is due to the large size of the molecule and the ligand oxygen and nitrogen atoms, which form coordination and ionic bonds with Pd(II) ions. The structure of **4c** is further investigated using X-ray diffraction structure analysis. The structural, spectral, and electronic transition properties were confirmed by measuring the UV-vis spectra and using theoretical techniques, like DFT and TD-DFT. Complexes **4a–j** were studied for their thermal characteristics using thermogravimetric analysis.

A useful method for determining different functional groups and their vibrational frequencies in free ligands and verifying their coordination with the central metal ion is infrared spectroscopy.[12,53,54] Functional group characteristics were evaluated, and their interaction with the Pd(II) centre was confirmed by recording the IR spectra of the ligands and their matching Pd(II) complexes within the 4000–400 cm^{-1} range. Prominent absorption bands observed between 1618 and 1420 cm^{-1} in the free ligands, attributed to ν(C=O), ν(C=C), and/or ν(C=N) stretching frequencies, support the formation of Schiff base **3a–j** (Table S1 and Fig. S1–S10).[12,53,54] In the synthesized complexes, the characteristic peaks were displaced to the 1592–1598 cm^{-1} range, indicating a decrease in the electron density of the carbonyl group as a result of its coordination with the Pd(II) ion. This coordination involves the donation of a lone pair of electrons (Table S1 and Fig. S11–S20).[12,53,54] Furthermore, for the uncoordinated ligands, the ν(N–H) vibration manifested as a prominent absorption band between 3100 and 3350 cm^{-1}.[75–77] These bands disappeared upon complexation, which demonstrates the deprotonation of the aniline hydrogen and provides evidence that the imine nitrogen is bound to the Pd(II) centre.[12,53,54] Moreover, the ν(C–O) and ν(C–N) stretching frequencies were observed to shift toward lower wavenumbers in the complexes, confirming the involvement of both oxygen and nitrogen donor atoms in metal coordination.[78–80] The emergence of new absorption bands attributed to ν(Pd–N) and ν(Pd–O) vibrations further validates the coordination of the carbonyl oxygen and imine nitrogen to the Pd(II) ion.[12,53,54,81]

The NMR spectra of both the ligands and their Pd(II) complexes were obtained in deuterated chloroform ($CDCl_3$), and the detailed data are shown in the SI (Tables S2, S3, and Fig. S21–S60). The methine (HC=C) protons in ligands **3a–j** appeared as singlets within the range of 5.14–5.21 ppm in their ^{1}H NMR spectra.[63–72] Upon coordination with Pd(II), these signals shifted slightly upfield to 4.81–4.86 ppm in the Pd(II) complexes **4a–j**,[12,53,54] which can be attributed to the shielding influence of the Pd(II) center as well as conformational modifications accompanying chelation. This behavior corroborates the IR spectral results, where the (C=O), (C=C), and/or (C=N) stretching vibrations were observed to shift toward lower wavenumbers, confirming the participation of the nitrogen and oxygen atoms in metal coordination.

The aromatic proton coupling patterns for both the free ligands and their complexes remained within the expected chemical shift region, displaying JHH coupling constants in the range of 6.4–8.5 Hz.[12,53,54,63–72] In the spectra of ligands **3a–j**, the amine (NH) proton resonances appeared between 12.49 and 11.84 ppm but disappeared entirely upon complexation, indicating deprotonation and subsequent coordination of the nitrogen atom to the Pd(II) ion.[12,53,54,75–77] This finding is further supported by IR analysis, where the absence of the ν(N–H) stretching band in the complexes provides additional evidence for imine nitrogen coordination.[12]

In Pd(II) complexes **4a–j**, the backbone methyl protons were observed as singlets between 1.40 and 1.60 ppm, showing a slight upfield shift relative to the corresponding ligand signals. The $^{13}C\{^1H\}$ NMR spectra of the ligands exhibited downfield carbonyl (C=O) signals in the region of 196.5–195.5 ppm for compounds **3a–j**. After coordination with Pd(II), this resonance shifted to a higher field between 176.9 and 175.9 ppm for complexes **4a–j**, which is consistent with the shielding effect produced by the metal center. This observation substantiates coordination through the imine nitrogen and carbonyl oxygen atoms, which is in agreement with previously reported Pd(II) complexes.[12,53,54,75–77] All remaining organic substituents displayed their expected chemical shifts without anomalous deviations.

Molecular ion peaks $[M + H]^+$ were observed for all complexes **4a–j** (Fig. S61–S71). HRMS (ESI^+) analysis of the complexes reveals well-defined isotopic clusters corresponding to the protonated molecular ions $[M + H]^+$, arising from the natural isotopic distribution of palladium. For $C_{24}H_{29}N_2O_2Pd$ (**4a–c**), an isotopic envelope is observed in the *m*/*z* 479–489 range. Complexes with the formula $C_{26}H_{33}N_2O_2Pd$ (**4d–f**, **4h**, and **4i**) display characteristic clusters in the *m*/*z* 507–516 range, while complex $C_{28}H_{37}N_2O_2Pd$ (**4g**) shows an isotopic pattern in the *m*/*z* 535–545 range. In addition, the dichloro complex $C_{24}H_{27}Cl_2N_2O_2Pd$ (**4j**) exhibits a distinctive isotopic envelope in the *m*/*z* 549–557 range (Table S4). The results obtained from the elemental (CHN) analysis of these complexes closely match the theoretically calculated values (Experimental section).

2.2. Crystal structures

Single crystals of complex **4c** were obtained by slow evaporation of a chloroform solution. The molecular structure is illustrated in Fig. 1, and the selected bond lengths and angles around the Pd(II) center are listed in Tables S6 and S7, respectively.

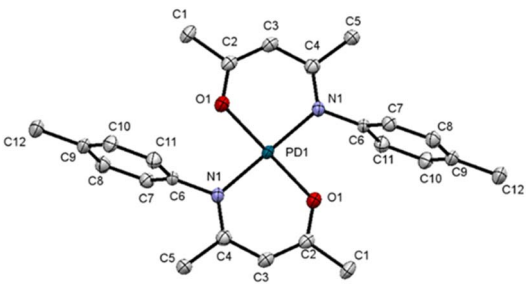

Fig. 1 ORTEP (50% probability level) of the molecular structure of **4c** with an atom-numbering scheme. Hydrogen atoms are omitted for clarity. Symmetry operation for generating the equivalent atoms: $-x + 1$, $-y + 1$, $-z + 1$.

Complex **4c** crystallizes in the triclinic space group $P\bar{1}$, with the asymmetric unit containing half of the molecule and the Pd(II) atom positioned at a crystallographic inversion center (Table S5). The ligand binds to the metal in a bidentate manner *via* the imine nitrogen and carbonyl oxygen atoms from two neighboring ligands. The coordination environment around the Pd(II) center adopts a slightly distorted square-planar geometry, characterized by a bond angle of 92.50(12)°. The C2–C3 and C3–C4 bond distances fall between the typical single and double bond values, suggesting the delocalization of the C=C π-electrons within the ligand backbone. The observed C2–O1 bond length of 1.272(5) Å is longer than that of a conventional C=O double bond (1.23 Å), implying partial electron delocalization throughout the ligand system.[71] The Pd–N bond distance (2.031(3) Å) is marginally longer than the Pd–O bond distance (1.991(3) Å), which is consistent with the established coordination characteristics. These structural parameters align well with the literature values reported for analogous palladium complexes.[12,53,54]

Within the crystal lattice of **4c**, CH···π interactions (2.880 Å) contribute to structural stabilization, as depicted in Fig. S72.[82–84] Geometry optimization of complex **4c** was carried out using the PBE0/def2-TZVP computational level combined with the CPCM solvation model ($CHCl_3$), and the optimized structure was compared with the experimental X-ray crystallographic data. The optimized geometric parameters for **4c**, listed in Tables S6 and S7, show excellent agreement with the experimentally determined bond lengths and angles.

2.3. Hirshfeld surface analysis

Hirshfeld surface analysis was employed to examine and compare the intermolecular interactions present within the crystal structure of complex **4c**. This technique highlights the regions where weak intermolecular forces occur and provides quantitative data on the atom···atom short contacts responsible for such interactions.[85] For complex **4c**, the Hirshfeld surfaces were mapped over d_{norm}, shape index, curvedness, and fragment patch parameters. To enhance the visualization of the molecular framework, the surfaces were rendered transparent (Fig. S73).

The corresponding 2D fingerprint plots (Fig. S74) illustrate the nature and intensity of the various intermolecular interactions and contact types within the crystal lattice. A prominent feature observed is the extensive H···H contact region, indicating strong van der Waals contributions. Moreover, a considerable C···H contact surface is evident in **4c** (Fig. S74c), corroborating the presence of CH···π interactions observed in the crystal packing (Fig. S75). Additional O···H, Pd···H, and H···N contact regions are also identified, further emphasizing the complex network of weak interactions stabilizing the structure. Comparable interaction patterns have been documented for related palladium complexes.[13,50,51]

In the intermolecular topology network of complex **4c**, molecules displayed in identical colors represent those participating in the same interaction network (Fig. S76). Each color corresponds to a distinct symmetry operation (Sym op), and the centroid–centroid distances (R) associated with these interactions are listed in Table S8. The most prominent interaction within the structure occurs at $R = 7.84$ Å, followed by another notable contact at $R = 7.49$ Å. In general, an inverse correlation is observed between the centroid distance (R) and the total interaction energy (E_{tot}), where smaller R values are associated with higher E_{tot} magnitudes. However, the interaction at $R = 13.42$ Å deviates from this pattern, indicating that stronger interaction energies are predominantly found at shorter centroid se*para*tions.

The total interaction energy (E_{tot}) is expressed in eqn (1), derived after applying a perturbation that enables its decomposition into individual energy components as follows:

$$E_{tot} = E_{ele} + E_{pol} + E_{dis} + E_{rep}, \quad (1)$$

where E_{ele}, E_{pol}, E_{dis}, and E_{rep} denote the electrostatic, polarization, dispersion, and repulsive energy components, respectively.[86] The energy framework for molecular pairs within the topological network of each crystal unit is depicted in Fig. S77. Consistent with the observations from the two-dimensional fingerprint plot analysis, this framework is constructed by linking the atoms involved in intermolecular interactions throughout the crystal lattice.

2.4. DFT calculations and electronic structures

Time-dependent density functional theory (TD-DFT) calculations were carried out to determine the vertical excitation energies and gain deeper insight into the electronic characteristics of the enaminone-based ligands (**3a–j**) and their corresponding Pd(II) complexes (**4a–j**). The computed absolute energies of the frontier molecular orbitals (HOMO and LUMO), along with the associated HOMO–LUMO energy gaps for **3a–j** and **4a–j**, are summarized in Tables S9 and S10. The main electronic transitions for the ligand and complex series for **3a–j** and **4a–j** are listed in Tables S11 and S12, respectively.

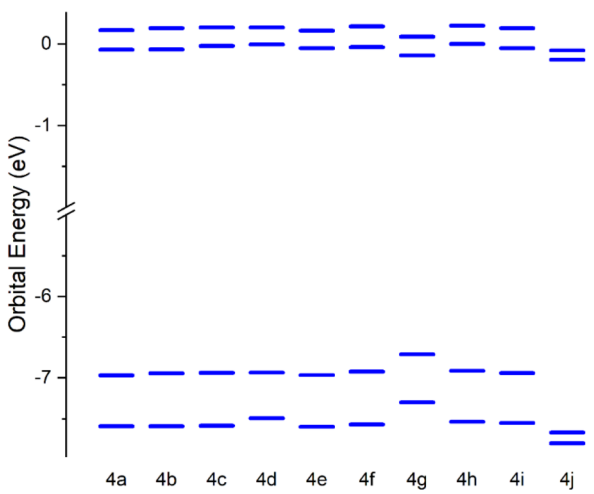

Fig. 2 Calculated HOMO−1, HOMO, LUMO and LUMO+1 energies of **4a–j**.

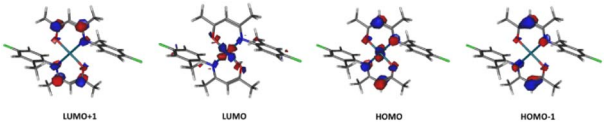

Fig. 3 Isosurface densities of the frontier orbitals, LUMO+1, LUMO, HOMO and HOMO−1, of the compound **4j** (isosurface value = 0.06).

A schematic diagram illustrating the relative frontier orbital energy levels for complexes **4a–j** is presented in Fig. 2. It is evident that in complexes containing one or two methyl substituents on the aryl ring (**4a–f**, **4h** and **4i**), the HOMO−1, HOMO, LUMO, and LUMO+1 orbitals possess nearly identical absolute energy values, resulting in an almost constant HOMO–LUMO energy gap (Fig. 2 and Table S10). In contrast, the substitution of one methyl group by a chlorine atom in compound **4j** leads to the stabilization of these orbitals, a consequence of the electron-withdrawing effect of chlorine. Interestingly, for compound **4g**, which contains three methyl substituents, the HOMO−1 and HOMO orbitals are destabilized, whereas the LUMO and LUMO+1 orbitals exhibit stabilization.

As illustrated in Fig. 3 for complex **4j**, the HOMO−1 orbitals are primarily localized on the two enaminone ligands, while the HOMO orbitals are delocalized over both the enaminone ligands and the Pd(II) center. The LUMO orbitals are mainly concentrated on the palladium atom, while the LUMO+1 orbitals are largely distributed over the enaminone ligands. This pattern of orbital localization is consistently maintained throughout the entire series of complexes, as depicted in Fig. S78–S87.

2.5. UV-visible absorption studies

The electronic absorption spectra of the ligands and their corresponding Pd(II) complexes were recorded in chloroform, and the combined spectra are presented in Fig. S88–S97. The ligands **3a–j** exhibited a single absorption band in the range of 310–327 nm, which can be assigned to $\pi \rightarrow \pi^*$ electronic transitions (Table S11).[87] Upon complexation with Pd(II), these bands underwent a bathochromic shift to 335–342 nm and showed reduced intensities, indicating a hypochromic effect (Table S12 and Fig. 4). This red shift likely arises from conformational changes associated with coordination to the Pd(II) center. Additionally, new broad absorption bands appeared between 400 and 436 nm in the spectra of the complexes, corresponding to spin-allowed $^1A_1g \rightarrow {}^1B_1g$ transitions, which are characteristics of square-planar geometries.[88] These spectral observations further support the square-planar coordination environment around the Pd(II) ion, which is consistent with single-crystal X-ray diffraction data.[89,90]

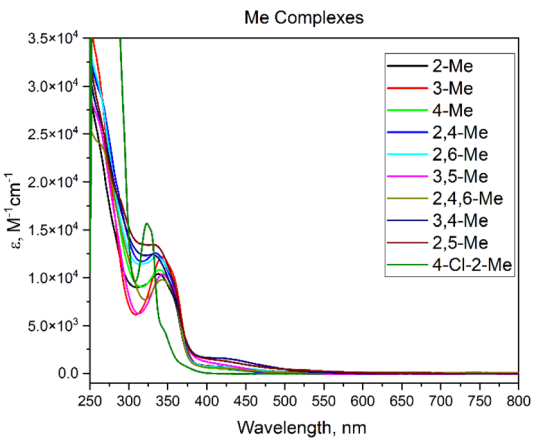

Fig. 4 Electronic absorption spectra ($CHCl_3$ and ambient temperature) of **4a–j**.

The overall spectral features closely resemble those reported for other square-planar Pd(II) complexes derived from Schiff-base ligands.[91,92] The measured molar extinction coefficients (ε) ranged from 1.0×10^4 to 2.2×10^4 M^{-1} cm^{-1}, suggesting that the observed bands originate from intra-ligand charge transfer (ILCT) transitions.[93] TD-DFT calculations, performed using the optimized geometries of the ligands and complexes, reproduced these experimental absorption features. The calculated and observed maximum absorption wavelengths (λ_{max}) for compounds **3a–j** and **4a–j** were in close agreement (Tables S11 and S12). For complexes **4a–j**, the dominant electronic transitions correspond to excitations from HOMO−1 to LUMO+1, while for free ligands **3a–j**, the transitions occur mainly from HOMO to LUMO, resulting in relatively higher-energy absorptions.[94] Consequently, the intense absorption bands observed for the Pd(II) complexes for **4a–j** in the UV-vis region are attributed to intra-ligand charge transfer (ILCT) transitions, as corroborated by the TD-DFT computational results.[95]

2.6. Thermogravimetric analysis

The TGA of Pd(II) complexes **4a–j** was carried out over a temperature range of 25 °C to 900 °C (Table S13), with individual thermograms presented in Fig. S100–S109. Complexes **4a–j** displayed a gradual weight loss as the temperature increased, indicating stepwise decomposition. All compounds were thermally stable up to approximately 220 °C, after which they began to decompose, with the observed weight losses corresponding to ligand dissociation, followed by the formation of PdO.

2.7. Anticancer activity

The biological evaluation of two groups of compounds, the methyl-substituted $[Pd(CH_3C(NAr)CHC(O)CH_3)_2]$ (**4**) (Ar = 2-methylphenyl (**a**); 3-methylphenyl (**b**); 4-methylphenyl (**c**); 2,4-dimethylphenyl (**d**); 2,6-dimethylphenyl (**e**); 3,5-dimethylphenyl (**f**); 2,4,6-trimethylphenyl (**g**); 3,4-dimethylphenyl (**h**); 2,5-dimethylphenyl (**i**); and 4-chloro-2-methylphenyl (**j**)) and the chloro-substituted $[Pd(CH_3C(NAr)CHC(O)CH_3)_2]$ (**5**) (Ar = 2-chlorophenyl (**a**); 3-chlorophenyl (**b**); 4-chlorophenyl (**c**); 2,4-dichlorophenyl (**d**); 2,6-dichlorophenyl (**e**); 3,5-dichlorophenyl (**f**); 2,4,6-trichlorophenyl (**g**); 2,3-dichlorophenyl (**h**); and 2,4,5-trichlorophenyl (**i**)),[12] was carried out using three cell lines: normal fibroblasts, breast cancer (MCF-7), and colon cancer (HCT-116). The cytotoxic responses of complexes **4a–j**, their corresponding

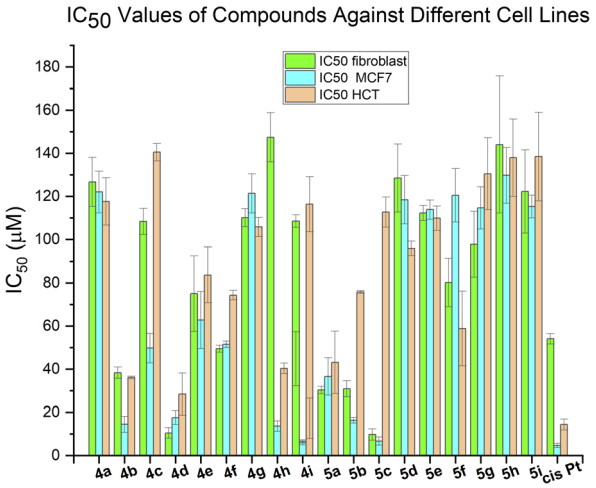

Fig. 5 Combined histogram showing the IC_{50} values of the Pd(II) complexes **4** and **5** against the MCF-7 and HCT-116 cell lines.

ligands on cell viability and corresponding IC_{50} values after 48 hours of incubation are displayed in Fig. 5, Tables S14 and S15, respectively.

Overall, several compounds displayed substantial cytotoxic effects, with a pronounced activity toward the MCF-7 cell line. Within the methyl-substituted group, compound **4i** was found to be the most effective against MCF-7 cells (IC_{50} = 5.42 μM), showing moderate inhibition of HCT-116 cells (IC_{50} = 17.20 μM) and minimal cytotoxicity toward fibroblasts (IC_{50} = 44.73 μM), which confirms its selectivity for cancerous cells. Likewise, compound **4j**, containing both methyl and chloro substituents, exhibited preferential cytotoxicity against MCF-7 (IC_{50} = 6.70 μM) while remaining inactive toward fibroblasts and HCT-116 cells.

In the chloro-substituted series, compound **5c** demonstrated the highest activity, with IC_{50} values of 6.71 μM for MCF-7 and 9.78 μM for fibroblasts, indicating strong cytotoxic behavior but slightly reduced selectivity relative to **4i** and **4j**. Compound **4d** also exhibited intermediate cytotoxic potency across all tested lines, with IC_{50} values of 10.48, 17.55, and 28.41 μM for fibroblasts, MCF-7, and HCT-116, respectively. Additional methyl derivatives, such as **4b**, **4h**, and **4c**, displayed moderate to good activity toward MCF-7, with IC_{50} values in the range of 13–50 μM, while their chloro analogues (**5b** and **5f**) showed comparable or slightly lower potency.

In contrast, compounds containing bulky or multiple substituents, including **4g**, **5e**, **5h**, and **5i**, were inactive across all tested cell lines (IC_{50} > 100 μM), suggesting that excessive steric crowding or substituent effects may hinder biological activity. Among all compounds, **4i**, **4j**, and **5c** emerged as the most promising candidates due to their strong cytotoxic potential and favorable selectivity profiles. In particular, **4i** demonstrated potent anticancer activity with minimal impact on normal fibroblasts. These findings highlight the significance of substitution patterns, especially at the 2- and 5-positions with methyl or chloro groups in modulating cytotoxic potency and selectivity.

Comparison of the present results with previously reported analogues $[Pd(CH_3C(NAr)CHC(O)Ph)_2]$ (**6**) (Ar = methyl-substituted phenyl)[53] and (**7**) (Ar = chloro-substituted phenyl)[54] revealed that complexes based on $[Pd(CH_3C(NAr)CHC(O)Ph)_2]$ exhibited distinct cytotoxic behavior compared to those derived from $[Pd(CH_3C(NAr)CHC(O)CH_3)_2]$, as summarized in Table S16.[53,54] The position and type of substituents on the aromatic ring had a pronounced effect on cytotoxic activity against MCF-7 breast cancer cells.

A clear structure–activity relationship (SAR) was observed when comparing compounds containing methyl (Me), chloro (Cl), and mixed substituents. Compound (**4a**) was inactive (IC_{50} > 100 μM), whereas its 2-chloro analogue (**5a**) showed moderate activity (IC_{50} = 36.57 μM). In contrast, compound (**6a**) (2-methyl) demonstrated slightly better cytotoxicity (IC_{50} = 35.61 μM), while (**7a**) (2-chloro) was inactive, suggesting only modest influence from 2-position substitution. The *meta*-substituted compound (**4b**) (3-methyl) displayed the highest activity among mono-methyl derivatives (IC_{50} = 14.49 μM), with its chloro counterpart (**5b**) (3-chloro) also showing good activity (IC_{50} = 16.39 μM), whereas (**6b**) and (**7b**) (3-substituted analogues) were inactive. This implies that *meta*-substitution enhances cytotoxicity mainly in simpler molecular scaffolds.

A significant improvement in potency was observed at the 4-position, particularly with chlorine substitution. Compound (**5c**) (4-Cl) was highly potent (IC_{50} ≈ 6.71 μM), while (**7c**) (4-Cl) showed moderate activity (IC_{50} = 49.62 μM) and (**4c**) (4-Me) weak activity (IC_{50} = 49.75 μM); compound (**6c**) (4-Me) was inactive. These findings highlight that *para*-chlorination substantially enhances cytotoxicity in simpler ligand systems. The 2,4-dimethyl compound (**4d**) exhibited moderate activity (IC_{50} = 17.55 μM), whereas (**5d**) (**6d**), and (**7d**) (2,4-dichloro or 2,4-dimethyl analogues) were inactive or weakly active, suggesting that *ortho–para* dimethyl substitution is advantageous mainly in less complex frameworks.

Compound (**4e**) (2,6-dimethyl) exhibited weak activity, while its dichloro analogues (**5e**) and (**6e**) (2,6-dichloro) were inactive (IC_{50} > 100 μM), indicating that *ortho–ortho* substitution reduces cytotoxicity, likely due to steric hindrance. The *meta*-dimethyl derivative (**4f**) (3,5-dimethyl) showed low activity (IC_{50} = 51.5 μM), while (**5f**) and (**7f**) (3,5-dichloro) were inactive, confirming that *meta–meta* substitution patterns are unfavorable.

Compounds (**4g**) (**5g**), and (**6g**), with substitutions at all *ortho* and *para* positions, were completely inactive, reinforcing that bulky or symmetric substitution limits cytotoxic potential. The *meta–para* disubstituted compound (**4h**) (3,4-dimethyl) showed notable activity (IC_{50} = 13.64 μM), whereas (**6h**) (3,4-dimethyl analogue) and (**7h**) (3,4-dichloro analogue) were inactive. This suggests that 3,4-substitution may impart beneficial electronic effects though these depend strongly on the molecular framework.

The *ortho–meta* disubstituted compound (**4i**) (2,5-dimethyl) exhibited excellent cytotoxicity (IC_{50} = 5.42 μM), while its analogue (**6i**) was inactive, demonstrating that the favorable substitution pattern is diminished in more rigid scaffolds. Compound (**4j**) (4-Cl-2-Me) also displayed strong activity (IC_{50} = 6.70 μM), further confirming that *para*-chlorination combined

with *ortho*-methyl substitution enhances potency. Compounds (**5h**) and (**7i**) (2,3-dichloro) and (**5i**) and (**7l**) (2,4,5-trichloro) were largely inactive although (**7l**) showed moderate cytotoxicity (IC_{50} = 33.88 μM), indicating that multiple chloro groups can yield modest activity depending on their orientation. The unsubstituted compound (**7m**) was weakly active (IC_{50} = 81.05 μM), and the ethyl-substituted derivative (**6n**) (2-Et) was inactive (IC_{50} > 400 μM), underscoring the importance of specific electron-donating or withdrawing substituents rather than simple alkylation for biological effectiveness.

Cisplatin, a palladium-based chemotherapy medication, exhibits IC_{50} values of 4.7 ± 0.97 against MCF7, 14.38 ± 2.5 against HCT116, and 54.02 ± 2.46 against fibroblast cells. Compared with our novel palladium complex anticancer activity, several complexes were able to achieve very similar results, such as compounds **4i** and **4j** (Fig. 5).

UV-vis measurements of the most active Pd(II) complex **4i** in media revealed no significant spectral changes over the monitored period, indicating satisfactory solution stability and an appreciable half-life under near-physiological conditions (Fig. S110).

HPLC provides precise quantitative results of samples in solutions and ensures the consistent quality of the products, meeting their regulatory requirements, because it delivers repeatable results across different batches. To further assess the stability of complex **4i**, we analyzed its aqueous solutions using the proposed HPLC procedure.[96,97] Complex **4i** was dissolved at a 20 μM concentration in a 3% DMSO media solution and injected as described in the Experimental section. The chromatograms were collected (Fig. S111), showing that the signal from the freshly prepared solutions remained practically unchanged over time. We graphically plotted the stability as the percentage of intact complex remaining, with the initial amount ($t = 0$) set as 100%. The integral of the signal corresponding to the complexes only slightly diminished after 72 h (89%).

2.8. Docking studies

As the anticancer efficacy of the newly synthesized Pd(II) complexes was assessed against breast cancer (MCF-7) and colon cancer (HCT-116) cell lines, the top 20 genes linked to each cancer type were examined using the COSMIC database.[98] In the breast cancer (MCF-7) model, only PIK3CA (E545K) and ERBB4 (Y1242C) were found to possess somatic mutations for which representative crystal structures were available. In the HCT-116 cell line, KRAS (G13D), PIK3CA (H1047R), and ATM (A112V) satisfied the same criteria. Consequently, molecular docking analyses were conducted by employing the PIK3CA-E545K mutant structure (PDB ID: 8GUD),[99] ERBB4-Y1242C (PDB: 2R4B),[100] KRAS-G13D (PDB: 8UN5),[101] PIK3CA-H1047R (PDB: 8TGD),[102] and ATM-A112V (PDB: 7NI5).[103]

The PIK3CA gene encodes the p110α catalytic subunit of phosphoinositide 3-kinase (PI3K), a lipid kinase responsible for regulating essential cellular activities, such as proliferation, metabolism, and survival.[104] Mutations in PIK3CA, particularly the E545K substitution within the helical domain, are commonly detected in numerous breast cancer cases.[102] This mutation leads to persistent activation of the PI3K/AKT/mTOR signaling cascade, thereby promoting oncogenic transformation of mammary epithelial cells.[105] Moreover, the E545K alteration has been associated with resistance to chemotherapy in triple-negative breast cancer due to its suppression of apoptosis and stimulation of pro-survival signaling pathways.[105]

ERBB4, also referred to as HER4, is a receptor tyrosine kinase that belongs to the epidermal growth factor receptor (EGFR) family. It interacts with neuregulins and other EGF-like ligands and plays a vital role in neural and cardiovascular development, as well as mammary gland differentiation.[106] Mutations in ERBB4 have been observed in several human malignancies, including breast carcinoma, highlighting its probable role in tumorigenesis.

KRAS functions as a small GTPase that conveys growth-promoting signals from surface receptors to downstream effectors, including the RAF–MEK–ERK and PI3K–AKT pathways, supporting cell survival and proliferation.[107,108] Both KRAS and PI3K are pivotal components in mitogenic signaling, with KRAS capable of directly activating PI3K, thereby intensifying downstream proliferative and survival mechanisms.[109]

ATM is a serine/threonine kinase that is activated in response to DNA double-strand breaks. It plays a vital role in preserving genomic stability by regulating DNA repair processes, enforcing cell-cycle checkpoints, and inducing apoptosis when necessary.[110] Once activated, ATM phosphorylates several downstream substrates to trigger cell-cycle arrest or promote DNA repair mechanisms. Loss or dysfunction of ATM leads to chromosomal instability and substantially increases the likelihood of cancer development.[111]

Mutations within KRAS, PIK3CA, and ATM proteins are key drivers of colorectal cancer (CRC). The KRAS-G13D mutation impairs GTP hydrolysis, resulting in the continuous activation of downstream signaling cascades.[109] The PIK3CA-H1047R mutation, located in the kinase domain, enhances catalytic activity and strengthens AKT signaling, thereby facilitating tumor growth.[112] These alterations work synergistically to promote highly aggressive and treatment-resistant CRC phenotypes.[109] Although the ATM-A112V variant has been less extensively characterized, it may compromise ATM's DNA repair function. ATM mutations are frequently detected in CRC and are associated with genomic instability and heightened cancer susceptibility.[104] The A112V alteration could potentially disrupt ATM's structural integrity or enzymatic activity, weakening the DNA damage response and contributing to colorectal tumorigenesis.[104,111]

Fig. 6 and 7 illustrate the binding energies of the Pd(II) complexes, while Tables S17 and S18 provide a summary of the binding energy values of these complexes against the five oncogenic protein targets. Overall, the docking scores for the breast cancer-associated proteins ranged from −4.386 to −8.469 kcal mol^{-1}, reflecting low to high binding affinity, while those for the colon cancer-associated proteins ranged from −4.514 to −7.915 kcal mol^{-1}, indicating low to moderate affinity. The results demonstrate distinct structure–activity correlations for each protein target.

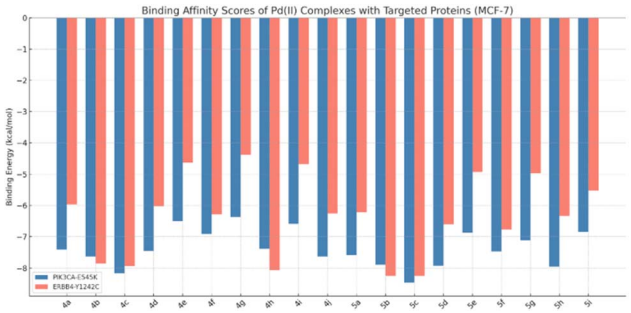

Fig. 6 Combined histogram displaying the binding energy scores of the Pd(II) complexes **4** and **5** against two targeted proteins (PIK3CA-E545K and ERBB4-Y1242C) in MCF-7 cells. Note: docking energies are presented for comparison with cell-based activity. No statistical correlation or regression analysis between these two datasets was performed in this study.

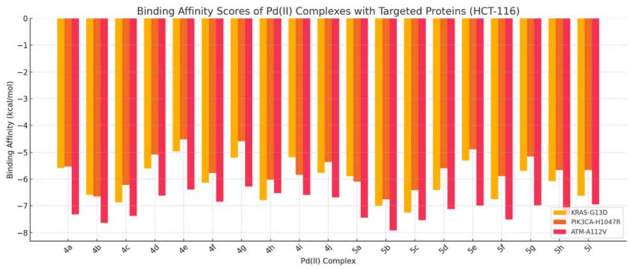

Fig. 7 Combined histogram displaying the binding energy scores of the Pd(II) complexes **4** and **5** against the KRAS-G13D, PIK3CA-H1047R and ATM-A112V targeted proteins in HCT-116.

2.9. Docking against PIK3CA-E545K protein

For the PIK3CA-E545K target (a breast cancer-associated protein), the methyl-substituted complexes (refer to Table S17) exhibited binding energies ranging from −6.373 to −8.162 kcal mol^{-1}, corresponding to moderate to high binding affinity. Among these, complex **4c** (4-methylphenyl) demonstrated the strongest binding, with a score of −8.162 kcal mol^{-1}. Two other *para*-substituted derivatives, **4b** (3-methylphenyl) and **4j** (4-chloro-2-methylphenyl), showed moderate affinities, with docking scores of −7.640 and −7.639 kcal mol^{-1}, respectively. Conversely, the sterically crowded analogue **4g** (2,4,6-trimethylphenyl) displayed the weakest binding energy (−6.373 kcal mol^{-1}), emphasizing the adverse impact of multiple *ortho* substituents on fitting within the PIK3CA-E545K binding pocket. This trend indicates that a single *para* substituent promotes favorable interactions, while bulky *ortho* groups hinder optimal binding.

The chloride-substituted series exhibited a comparable trend but generally demonstrated stronger affinities (as summarized in Table S17). Notably, complex **5c** (4-chlorophenyl) produced the most favorable docking score among all the examined compounds (−8.469 kcal mol^{-1}). Other *para* and *meta*-substituted chlorides, including **5b**, **5d**, and **5h**, also showed relatively strong binding, with energies between −7.893 and −7.950 kcal mol^{-1}. In contrast, *ortho*-substituted chlorides, such as **5e** (2,6-dichlorophenyl) and **5i** (2,4,5-trichlorophenyl),

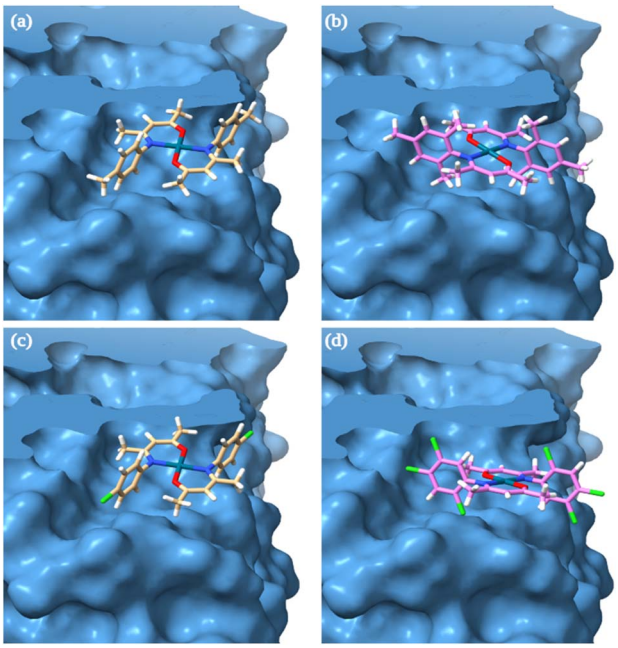

Fig. 8 Binding site in the PIK3CA-E545K protein occupied by the best- and worst-docked methyl- and chloride-substituted Pd(II) complexes: (a) **4c**, (b) **4g**, (c) **5c**, and (d) **5i**.

displayed weaker interactions, with scores of −6.870 and −6.847 kcal mol^{-1}, respectively. These observations suggest that substituting a methyl group with chlorine at the *para* position enhances protein affinity likely due to chlorine's higher polarizability and dispersion effects, while extensive *ortho* substitution continues to introduce steric hindrance that reduces binding efficiency.

Fig. 8 illustrates these binding modes. In the high-affinity poses (Fig. 8a and c), the aromatic ring of the **4c** and **5c** complexes points deeply into a hydrophobic cleft of PIK3CA-E545K, maximizing van der Waals contacts. In contrast, the low-affinity complexes **4g** and **5i** (Fig. 8b and d) cannot fit fully; their bulky *ortho* groups clash with the protein and force the ring out of the optimal position. The corresponding 2D interaction diagrams (Fig. S112) confirm that hydrophobic contacts dominate in all cases. No strong hydrogen bonds or electrostatic interactions were observed, emphasizing that binding is driven largely by nonpolar interactions with the pocket.

Taken together, for PIK3CA-E545K, docking suggests that analogues with a single *para* substituent (especially chloride) should bind most tightly. Because PIK3CA-E545K is an oncogenic driver in breast cancer, the strong-binding complexes (**4c** and especially **5c**) are prime candidates for inhibiting this target. Their predicted high affinity implies that they may effectively compete with ATP and disrupt PIK3CA protein signaling in the MCF-7 cell line, which is consistent with potential anticancer activity.

2.10. Docking against ERBB4-Y1242C protein

The ERBB4-Y1242C variant, also associated with breast cancer, exhibited a wide distribution of binding affinities (as shown in

Table S17). For the methyl-substituted series, docking scores ranged from −4.386 to −8.059 kcal mol^{-1}, corresponding to low through high affinity. The most potent ligand was **4h** (3,4-dimethylphenyl, −8.059 kcal mol^{-1}), featuring mixed *meta*/*para* substitution, while **4c** (4-methyl) also showed strong binding at −7.937 kcal mol^{-1}. In contrast, compounds with extensive *ortho* substitution, namely **4g** (2,4,6-trimethyl) and **4e** (2,6-dimethyl), demonstrated markedly weaker affinities at −4.386 and −4.623 kcal mol^{-1}, respectively. These reduced scores indicate that the relatively flat and elongated kinase groove of ERBB4-Y1242C cannot effectively accommodate bulky *ortho* groups, leading to suboptimal occupancy of the binding site.

Similarly, the chloride-substituted series displayed a range from −4.925 to −8.245 kcal mol^{-1}. The highest affinities were observed for **5b** and **5c** (3-chlorophenyl and 4-chlorophenyl), both scoring −8.245 kcal mol; each contains a single chlorine atom at the *meta* or *para* position. Conversely, **5e** (2,6-dichlorophenyl, −4.925 kcal mol^{-1}) and **5g** (2,4,6-trichlorophenyl, −4.970 kcal mol^{-1}) exhibited the weakest binding. This again highlights that multiple *ortho* substitutions, particularly in *ortho–para* configurations, significantly diminish binding affinity most likely due to steric interference within the ERBB4-Y1242C binding pocket.

Fig. 9 illustrates the representative binding poses of the selected ligands within the ERBB4-Y1242C active site. Complex **4h** (Fig. 9a) positions both methyl-substituted rings tightly along the hydrophobic groove, achieving optimal alignment, whereas **4g** (Fig. 9b) fails to orient correctly and binds more superficially, being displaced from the optimal site. Similarly, **5c** (Fig. 9c) fits comfortably within the binding pocket, while **5e** (Fig. 9d) experiences steric hindrance due to its two *ortho* chlorine substituents. The ligand–interaction diagrams (Fig. S113) demonstrate that **4h** and **5c** form numerous hydrophobic contacts with residues in the ATP-binding cleft, while **4g** and **5e** exhibit substantially fewer interactions. Notably, no hydrogen bonds were observed in any of the ERBB4-Y1242C complexes, indicating that binding is primarily mediated by dispersion (van der Waals) forces.

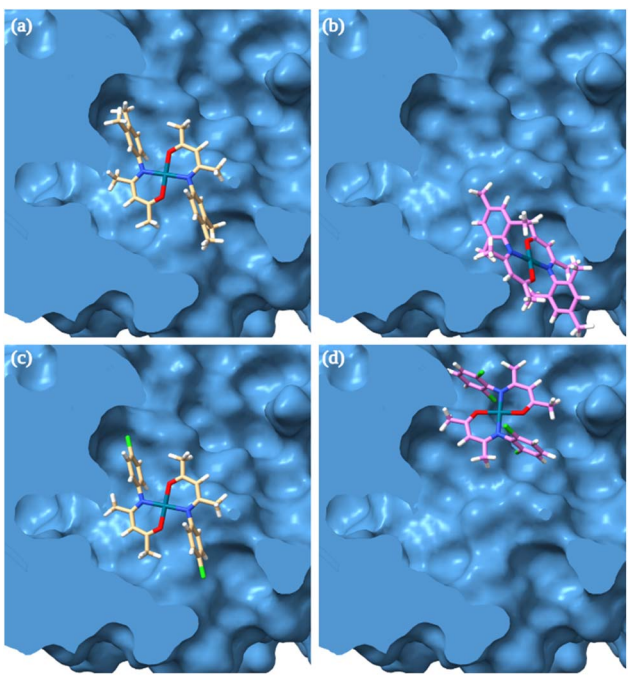

Fig. 9 Binding site in the ERBB4-Y1242C protein occupied by the best- and worst-docked methyl- and chloride-substituted Pd(II) complexes: (a) **4h**, (b) **4g**, (c) **5c**, and (d) **5e**.

These findings imply that the most potent ERBB4-Y1242C inhibitors are analogues resembling **4h** and **5c**/**5b**, whose strong hydrophobic engagement could disrupt abnormal EGFR family signaling in cancer cells, which is consistent with the potential anticancer activity observed in the MCF-7 cell line. In contrast, compounds, such as **4g** and **5e**, which fail to achieve stable pocket occupation, are unlikely to inhibit kinase activity effectively.

2.11. Docking against KRAS-G13D protein

For the KRAS-G13D target (a key mutant associated with colon cancer), the methyl-substituted series (Table S18) exhibited binding energy values ranging from −4.960 to −6.870 kcal mol^{-1}, corresponding to low-to-moderate affinity. The strongest binder was **4c** (4-methylphenyl) with a score of −6.870 kcal mol^{-1}, while the sterically congested analogue **4e** (2,6-dimethylphenyl) produced the weakest score (−4.960 kcal mol^{-1}). This difference highlights that a single *para* substituent favors optimal binding, whereas multiple *ortho* methyl groups create steric clashes that hinder proper accommodation within the KRAS-G13D binding site.

The chloride-substituted series followed a similar pattern but generally demonstrated stronger affinities, with binding energies ranging from −5.312 to −7.253 kcal mol^{-1} (Table S18). Among these, **5c** (4-chlorophenyl) achieved the most favorable value of −7.253 kcal mol^{-1}, representing the best overall binder. In contrast, *ortho*-substituted chlorides such as **5e** (2,6-dichlorophenyl) performed poorly, with a score of −5.312 kcal mol^{-1}. These results indicate that substituting methyl with chlorine at the *para* position enhances binding likely due to chlorine's higher polarizability and stronger dispersion interactions, while heavy *ortho* substitution continues to impose steric penalties.

Fig. 10 illustrates the representative binding poses for these complexes. In the high-affinity structures (Fig. 10a and c), the aromatic rings of **4c** and **5c** extend deeply into the hydrophobic cleft of KRAS-G13D, forming extensive van der Waals contacts. In contrast, low-affinity analogues **4e** and **5e** (Fig. 10b and d) fail to fit properly; their bulky *ortho* groups create steric clashes that push the ligands toward the pocket entrance and into solvent exposure. The corresponding 2D interaction diagrams (Fig. S114) confirm that hydrophobic interactions dominate across all complexes, with no significant hydrogen bonding or electrostatic contacts observed, indicating that binding is primarily driven by nonpolar forces.

Overall, the docking results for KRAS-G13D suggest that analogues containing a single *para* substituent, particularly chlorine, exhibit the most favorable binding profiles. Given that

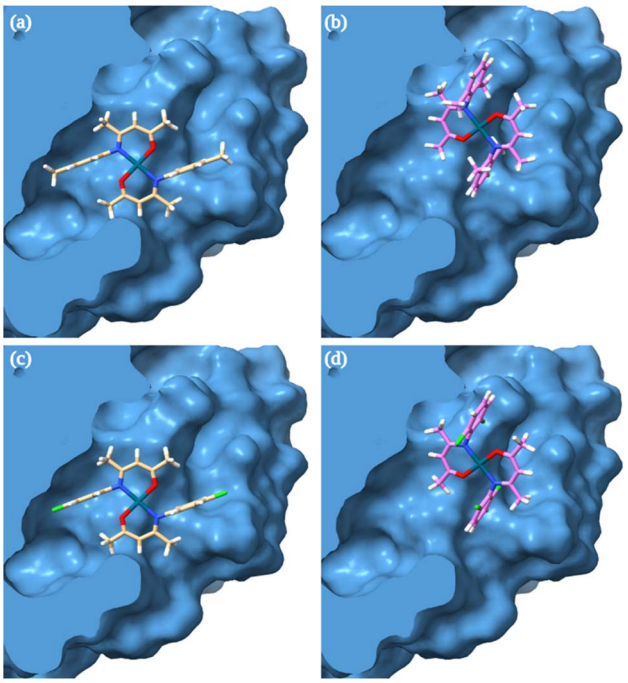

Fig. 10 Binding site in the KRAS-G13D protein occupied by the best- and worst-docked methyl- and chloride-substituted Pd(II) complexes: (a) **4c**, (b) **4e**, (c) **5c**, and (d) **5e**.

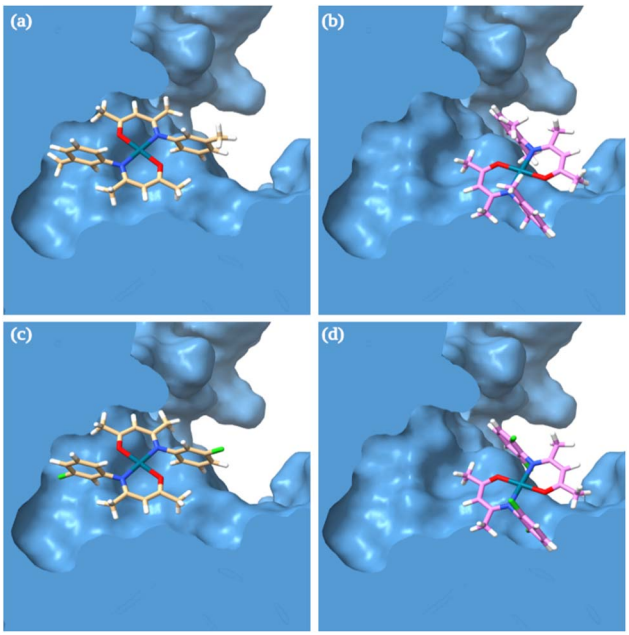

Fig. 11 Binding site in the PIK3CA-H1047R protein occupied by the best- and worst-docked methyl- and chloride-substituted Pd(II) complexes: (a) **4b**, (b) **4e**, (c) **5b**, and (d) **5e**.

KRAS-G13D is an oncogenic driver mutation in colon cancer, strong-binding compounds **4c** and especially **5c** emerge as promising candidates for disrupting KRAS-mediated MAPK signaling.

2.12. Docking against PIK3CA-H1047R protein

For the PIK3CA-H1047R target (another colon cancer–associated mutant), the methyl-substituted series (Table S18) exhibited binding energies ranging from −4.514 to −6.651 kcal mol^{-1}, indicating low-to-moderate affinity. The strongest binder in this set was **4b** (3-methylphenyl), with a score of −6.651 kcal mol^{-1}, while the most sterically hindered analogue, **4e** (2,6-dimethylphenyl), showed the weakest binding at −4.514 kcal mol^{-1}. This trend indicates that a single *meta* substituent promotes favorable interactions within the PIK3CA-H1047R binding site, while multiple *ortho* substituents introduce steric congestion that prevents optimal accommodation of the ligand in the pocket.

The chloride-substituted series followed a comparable pattern but demonstrated slightly stronger overall binding affinities, with docking scores ranging from −4.884 to −6.764 kcal mol^{-1} (Table S18). Among these, **5b** (3-chlorophenyl) exhibited the highest affinity with a score of −6.764 kcal mol^{-1}, representing the best binder in the set. In contrast, the *ortho*-substituted analogue **5e** (2,6-dichlorophenyl) yielded a much weaker score of −4.884 kcal mol^{-1}. These results suggest that the substitution of a methyl group by chlorine at the *meta* position enhances binding likely due to chlorine's higher polarizability and stronger dispersion forces, while multiple *ortho* substituents continue to cause steric interference that reduces ligand fit and affinity within the PIK3CA-H1047R binding site.

Fig. 11 depicts the representative binding conformations of the ligands within the PIK3CA-H1047R active site. In the high-affinity complexes (Fig. 11a and c), the aromatic rings of **4b** and **5b** are deeply inserted into a hydrophobic cleft of PIK3CA-H1047R, allowing for optimal van der Waals interactions. In contrast, low-affinity complexes **4e** and **5e** (Fig. 11b and d) are sterically hindered by their bulky *ortho* substituents, which prevent proper fitting and force the ligands toward the pocket entrance, resulting in partial solvent exposure. The corresponding 2D interaction diagrams (Fig. S115) confirm that hydrophobic interactions dominate across all complexes. No strong hydrogen bonds or electrostatic interactions were detected, indicating that ligand binding in PIK3CA-H1047R is primarily governed by nonpolar forces.

Collectively, the docking results for PIK3CA-H1047R indicate that analogues bearing a single *meta* substituent, particularly chlorine, exhibit the strongest binding affinity. Given that PIK3CA-H1047R is an oncogenic driver mutation in colon cancer, high-affinity complexes **4b** and especially **5b** emerge as promising candidates for inhibiting this target effectively.

2.13. Docking against ATM-A112V protein

For the ATM-A112V target (another colon cancer-associated mutant), the methyl-substituted series (Table S18) exhibited binding energy scores ranging from −6.283 to −7.641 kcal mol^{-1}, indicating moderate affinity. The strongest binder in this set was **4b** (3-methylphenyl) with a score of −7.641 kcal mol^{-1}, while the most sterically hindered analogue

4g (2,4,6-trimethylphenyl) showed the weakest binding at −6.283 kcal mol^{-1}. This trend indicates that a single *meta* substituent enhances binding, while multiple *ortho* methyl groups introduce steric crowding that limits optimal fitting within the ATM-A112V pocket.

The chloride-substituted series displayed a comparable pattern but generally demonstrated stronger binding, with energy scores ranging from −6.946 to −7.915 kcal mol^{-1} (Table S18). Among these, **5b** (3-chlorophenyl) achieved the most favorable score of −7.915 kcal mol^{-1}, representing the strongest binder overall. In contrast, **5i** (2,4,5-dichlorophenyl) exhibited the weakest affinity at −6.946 kcal mol^{-1}, reflecting the negative impact of extensive *ortho* and *meta* substitution. These findings suggest that replacing a methyl group with chlorine at the *meta* position improves binding likely due to chlorine's higher polarizability and enhanced dispersion interactions, while excessive substitution continues to impose steric hindrance.

Fig. 12 illustrates these binding modes. In the high-affinity complexes (Fig. 12a and c), the aromatic rings of **4b** and **5b** are deeply positioned within a hydrophobic cleft of ATM-A112V, maximizing van der Waals contacts. In contrast, the low-affinity complexes **4g** and **5i** (Fig. 12b and d) fail to fit properly due to steric clashes from bulky *ortho* groups, which displace the ligands toward the pocket entrance. The 2D interaction diagrams (Fig. S116) confirm that hydrophobic interactions predominate across all complexes, with no significant hydrogen bonding or electrostatic interactions observed, emphasizing that binding is primarily driven by nonpolar forces.

Overall, the docking results for ATM-A112V indicate that analogues featuring a single *meta* substituent, particularly chlorine, exhibit the strongest binding affinity. Since ATM-A112V is an oncogenic driver mutation in colon cancer, high-affinity complexes **4b** and especially **5b** emerge as promising candidates for effective inhibition of this target.

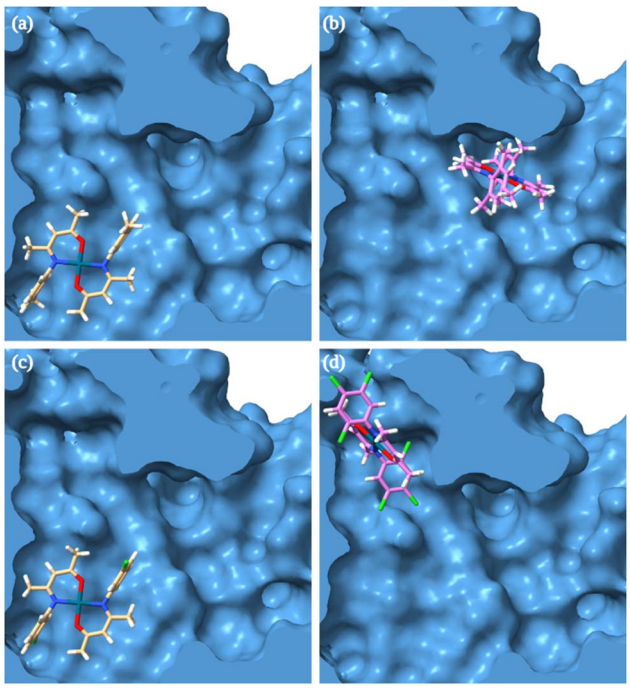

Fig. 12 Binding site in the ATM-A112V protein occupied by the best- and worst-docked methyl- and chloride-substituted Pd(II) complexes: (a) **4b**, (b) **4g**, (c) **5b**, and (d) **5i**.

2.14. Comparative analysis of docking results and cell-based selectivity

The docking results reveal qualitative agreement with some of the experimentally measured selectivity indices. We emphasize that these observations are descriptive: no quantitative statistical correlation was performed for the docking *versus* biological data, and no biochemical validation of the target engagement was carried out. Consequently, the docking results should be considered hypothesis-generating and used to guide future validation experiments rather than as proof of target inhibition. This relationship indicates that more favorable docking energies are generally associated with higher tumor-cell selectivity.

In the MCF-7 cell line, cytotoxicity assays identified four selective and two toxic complexes: **4b** (SI = 2.6), **4c** (SI = 2.2), **4h** (SI = 10.8), **4i** (SI = 8.3), **5b** (SI = 1.9), and **5c** (SI = 1.5). These compounds displayed moderate to high docking affinities toward PIK3CA-E545K and ERBB4-Y1242C, as summarized in Table S18. The four selective complexes (**4b**, **4c**, **4h**, and **4i**) share planar aryl–Pd(II) scaffolds with single *meta* or *para* substituents, which enable efficient hydrophobic interactions within the hinge region and deeper lipid-binding pockets. In contrast, **5b** and **5c**, although exhibiting the most negative docking scores, presented lower SI values, implying that extensive halogenation may increase nonspecific cytotoxicity despite favorable binding energies. These observations are consistent with independent natural-product studies reporting that planarity and hydrophobic surface area are key determinants of biological activity in MCF-7 models.[113,114]

In the HCT-116 cell line, cytotoxicity assays revealed only two selective complexes: **4h** (SI = 3.7) and **4i** (SI = 2.6). These compounds demonstrated low-to-moderate docking affinities against KRAS-G13D, PIK3CA-H1047R, and ATM-A112V, as shown in Table S16. For HCT-116, the pattern is less concordant: complexes with the most favorable docking scores did not consistently show the highest selectivity indices. This discrepancy underlines the important limitations of docking-to-cellular-activity comparisons: (i) docking assesses a static, structural interaction with an isolated protein and does not account for cellular uptake or efflux; (ii) metabolic transformation or decomposition may alter the active species; (iii) multiple intracellular targets and pathway crosstalk can determine cytotoxic outcomes; and (iv) protein expression and mutation context in a cell line may differ from the single crystal structure used for docking. Hence, docking results for HCT-116 are best interpreted cautiously and as pointers to possible binding modes rather than as predictors of cell-line potency.

Ligand speciation and biological relevance: palladium(II) complexes can be kinetically labile and may undergo aquation, solvent coordination, or ligand exchange in aqueous media; chelation by biomolecules and the formation of substituted species are well documented for Pd(II) chemistry. These

transformations can alter lipophilicity, charge, and the molecular surface presented to protein binding pockets and therefore influence biological outcomes. Our docking experiments modelled intact neutral complexes; readers should be aware that bioactive species inside cells may differ. We therefore interpret docking predictions as plausible binding hypotheses contingent on the intact complex (or a closely related species) reaching and interacting with the target protein.

2.15. Effect of compounds on apoptosis *via* qPCR

To evaluate the efficiency of the compounds over cell fate, the effects of one active (**4h**) and one inactive (**4a**) compound on apoptosis-related genes (Bax and Bcl-2) were assayed. For this purpose, 100 thousand cells of each MCF7 and HCT116 cancer cell type were seeded in a 12-well plate. Then, they were treated with the corresponding compound. Two concentrations of each compound were selected for this experiment based on the IC_{50} values of each compound for each cell line. The treated cells were cultured for 24 hours. Then, the total RNA was extracted using the RNeasy Plus Mini Kit (Qiagen). The amount of 1000 ng of RNA was converted to complementary DNA (cDNA) using the PrimeScript 1st strand cDNA Synthesis Kit (Takara). Real-time PCR was performed using Applied Biosystems™ PowerTrack™ SYBR Green Master Mix (ThermoFisher Scientific). Then, qPCR was performed to test the changes in the expression of apoptosis-related genes, Bax and Bcl-2. The 18S rRNA gene was used as a reference gene in this experiment. The primer sequences used are listed in Table S19.

The relative expressions of the pro-apoptotic gene Bax and the anti-apoptotic gene Bcl-2 were evaluated across fibroblast and cancer cell lines following treatment with different compound concentrations (Table S20). Changes in gene expression were quantified using $\Delta\Delta C_t$ analysis, and the Bax/Bcl-2 ratio was calculated as an indicator of apoptotic balance. In normal fibroblast cells, treatment resulted in generally low $\Delta\Delta C_t$Bax values, particularly at higher compound concentrations, while $\Delta\Delta C_t$Bcl-2 values remained comparatively higher. Consequently, the Bax/Bcl-2 ratio remained below or close to 1 in fibroblast cells, indicating a limited pro-apoptotic response under these conditions.

In contrast, cancer cell lines exhibited a marked increase in Bax expression relative to Bcl-2, and $\Delta\Delta C_t$Bax values were substantially elevated, while $\Delta\Delta C_t$Bcl-2 values were reduced, resulting in a pronounced increase in the Bax/Bcl-2 ratio, particularly at higher concentrations. In MCF-7 cells, compound **4h** reached $\Delta\Delta C_t$Bax: $\Delta\Delta C_t$BcL2 up to (12.3) at a high concentration, while compound **4a** had values around (1.5). A similar trend was observed in HCT116 cells, where treatment induced a strong shift toward pro-apoptotic signaling in active compound **4h**, as reflected by Bax/Bcl-2 ratios well above 1, while the inactive compound **4a** has values $\leq$1.

Overall, these findings demonstrate that compound **4h** selectively enhances pro-apoptotic gene expression in cancer cells while exerting minimal apoptotic effects in normal fibroblasts, suggesting a cancer-specific apoptotic response mediated through modulation of the Bax/Bcl-2 balance.

3. Conclusion

New palladium(II) complexes, $[Pd(CH_3C(NAr)CHC(O)CH_3)_2]$ (**4**) (Ar = 2-methylphenyl (**a**); 3-methylphenyl (**b**); 4-methylphenyl (**c**); 2,4-dimethylphenyl (**d**); 2,6-dimethylphenyl (**e**); 3,5-dimethylphenyl (**f**); 2,4,6-trimethylphenyl (**g**); 3,4-dimethylphenyl (**h**); 2,5-dimethylphenyl (**i**); and 4-chloro-2-methylphenyl (**j**)), were synthesized by reacting one equivalent of $[PdCl_2(NCCH_3)_2]$ with two equivalents of the corresponding substituted enaminone ligands in the presence of two equivalents of KO*t*Bu. The newly synthesized palladium complexes were characterized by IR, ^{1}H NMR, $^{13}C\{^1H\}$ NMR, elemental analysis, and UV-vis spectroscopy.

The X-ray crystallographic analysis of **4c** confirmed that the Pd(II) ion adopts a centrosymmetric square-planar geometry. Comparison of the experimental data with the optimized molecular geometries obtained from DFT/B3LYP calculations showed strong agreement. The HOMO−1 and LUMO+1 orbitals were mainly localized on the π and π^* systems of the enaminone ligands. TD-DFT calculations indicated that the single absorption band observed in the UV-vis spectra corresponded to ligand-to-ligand charge transfer (LLCT) transitions. Thermogravimetric analysis revealed a single major decomposition stage for all complexes, indicating similar thermal stability.

Biological evaluation demonstrated that **4i**, **4b**, **6c**, and **4j** exhibited low IC_{50} values against MCF-7 breast cancer cells. Among these, **4i** and **5c** emerged as the most promising candidates for further development due to their strong cytotoxic activity against both breast and colon cancer cell lines.

Comprehensive molecular docking studies on PIK3CA, ERBB4, KRAS, and ATM oncogenic targets revealed that the position and nature of aryl substituents critically influence binding strength. Complexes containing a single *meta* substituent or *para*-halogenation showed optimal van der Waals interactions, while heavily *ortho*-substituted analogues experienced steric hindrance at the binding site entrance. A qualitative correspondence between docking affinities (notably for PIK3CA-E545K) and some MCF-7 selectivity indices suggests that docking may be a useful tool for hypothesis generation and prioritizing analogues but should not be taken as predictive proof in the absence of quantitative correlation analysis or biochemical validation.

The apoptosis gene expression assay indicates that the active compound **4h** modulates apoptotic signaling in a cell type-dependent manner, as reflected by differential regulation of Bax and Bcl-2 expression. In normal fibroblast cells, the consistently low Bax/Bcl-2 ratios suggest that treatment does not substantially activate pro-apoptotic pathways, supporting a favorable safety profile in non-malignant cells. In contrast, both MCF-7 and HCT116 cancer cell lines exhibited a pronounced increase in the Bax/Bcl-2 ratio, which was driven primarily by the upregulation of Bax and/or suppression of Bcl-2, indicating a shift toward apoptosis. This effect was more evident at higher compound concentrations, suggesting a concentration-dependent pro-apoptotic response in malignant cells. Collectively, these results support the notion that

compound **4h** selectively promotes apoptosis in cancer cells while sparing normal fibroblasts likely through the disruption of the mitochondrial apoptotic balance, highlighting its potential therapeutic relevance as an apoptosis-inducing agent.

Overall, these findings provide valuable insights for the rational design of next-generation β-ketoiminato Pd(II) complexes, demonstrating that controlling substituent patterns can enhance target engagement and improve anticancer potency.

Author contributions

DT: conceptualization, manuscript writing with input from all authors, funding acquisition, resources, and supervision. BK, SA, ZI, WH, TAT, AI, MSS, TA and AM: investigation, data curation, and validation. MM: protein–ligand molecular docking simulations. MK: formal analysis, investigation, and single-crystal X-ray diffraction. All authors contributed to the discussion of results and provided comments on the manuscript.

Conflicts of interest

There are no conflicts to declare.

Data availability

CCDC 2478443 contains the supplementary crystallographic data for this paper.[115]

The raw data supporting the conclusions of this article will be made available by the corresponding authors upon request. Supplementary information (SI): experimental; IR (KBr) data for **3a–j** and **4a–j**; NMR (^{1}H, ^{13}C{^{1}H}) data for **3a–j**; analysis for each peak observed from HRMS for complexes **4a–j**; crystal data and structure refinement for compound **4c**; selected experimental and calculated bond distances (Å) for compound **4c**; selected experimental and calculated bond angles (°) for compound **4c**; interaction topology energy table for **4c** at the HF/3-21G level of theory; absolute HOMO and LUMO energies and the HOMO–LUMO gap for **3a–j** calculated at PBE0/def2-TZVP/CPCM (chloroform). Absolute HOMO and LUMO energies and the HOMO–LUMO gap for **4a–j** calculated at PBE0/def2-TZVP/CPCM (chloroform). Experimental and calculated [TD-CAM-B3LYP/def2-TZVP/CPCM (chloroform)] UV-vis absorption bands of ligands **3a–j** in chloroform solvent; experimental and calculated [TD-CAM-B3LYP/def2-TZVP/CPCM (chloroform)] UV-vis absorption bands of complexes **4a–j** in chloroform solvent; TGA data of **4a–j**; chemosensitivity results of complexes **4** and **5** against fibroblast, MCF-7 and HCT-116. Values are stated as 50% inhibitory concentrations (IC50) ± Standard Deviation (SD) and are triplicate repeats; chemosensitivity results of ligands against fibroblast, MCF-7 and HCT-116; chemosensitivity results of complexes **6** and **7**, against HT-29 and MCF-7; lowest binding energy values of methyl- and chloride-substituted Pd(II) complexes with targeted proteins in MCF-7 (breast cancer); lowest binding energy values of methyl- and chloride-substituted Pd(II) complexes with targeted proteins in HCT-116 (colon cancer); list of qPCR primers; Hirshfeld surface of 4c; full 2-D fingerprint plot for **4c**; Hirshfeld surface contacts in **4c**; the isosurface densities of the frontier orbitals: LUMO+1, LUMO, HOMO, HOMO−1 of compound **4a–j** and electronic absorption spectra ($CHCl_3$, ambient temperature) of **2a–j**, **3a–j** and **4a–j**. See DOI: https://doi.org/10.1039/d5ra09325b.

Acknowledgements

We gratefully acknowledge the University of Jordan for the financial support. The molecular docking studies were carried out using the High Performance Computing facilities at New York University, Abu Dhabi. The molecular graphics and structural analyses were performed using UCSF ChimeraX, developed by the Resource for Biocomputing, Visualization, and Informatics at the University of California, San Francisco, with support from the NIH grant R01-GM129325 and the Office of Cyber Infrastructure and Computational Biology, the National Institute of Allergy and Infectious Diseases.

References

1 L. H. Abdel-Rahman, M. S. S. Adam, A. M. Abu-Dief, H. Moustafa, M. T. Basha, A. S. Aboraia, B. S. Al-Farhan and H. E. Ahmed, *Appl. Organomet. Chem.*, 2018, **32**, e4527.
2 L. H. Abdel-Rahman, A. M. Abu-Dief, M. R. Shehata, F. M. Atlam and A. A. H. Abdel-Mawgoud, *Appl. Organomet. Chem.*, 2019, **33**, e4699.
3 A. M. Abu-Dief, L. H. Abdel-Rahman and A. A. H. Abdel-Mawgoud, *Appl. Organomet. Chem.*, 2020, **34**, e5373.
4 M. S. More, P. G. Joshi, Y. K. Mishra and P. K. Khanna, *Mater. Today Chem.*, 2019, **14**, 100195.
5 A. N. Kursunlu, E. Guler, F. Sevgi and B. Ozkalp, *J. Mol. Struct.*, 2013, **1048**, 476–481.
6 Md. A. Arafath, F. Adam, M. R. Razali, L. E. Ahmed Hassan, M. B. K. Ahamed and A. M. S. A. Majid, *J. Mol. Struct.*, 2017, **1130**, 791–798.
7 M. M. Abo-Aly, A. M. Salem, M. A. Sayed and A. A. Abdel Aziz, *Spectrochim. Acta, Part A*, 2015, **136**, 993–1000.
8 S. Kaya, S. Erkan and D. Karakaş, *Spectrochim. Acta, Part A*, 2021, **244**, 118829.
9 B. Iftikhar, K. Javed, M. S. U. Khan, Z. Akhter, B. Mirza and V. Mckee, *J. Mol. Struct.*, 2018, **1155**, 337–348.
10 Ö. Özdemir, P. Gürkan, Y. D. Şimay Demir and M. Ark, *J. Mol. Struct.*, 2020, **1207**, 127852.
11 V. S. V. Rani, T. Dhanasekaran, M. Jayathuna, V. Narayanan and D. Jesudurai, *Mater. Today: Proc.*, 2018, **5**, 8784–8788.
12 D. Taher, S. AlNaimat, K. I. Assaf, W. Helal and M. Korb, *Eur. J. Inorg. Chem.*, 2025, **28**, e202400730.
13 M. W. Amer, E. M. Khdeir, F. Barzagli, M. A. Taha, H. M. Alsalti, E. N. Ibrahim, R. A. Almassi, A. R. Hasoneh, M. Y. Rasheed and R. Al-Jawasrah, *Environ. Prog. Sustainable Energy*, 2024, **43**, e14469.
14 M. W. Amer, J. S. Aljariri Alhesan, M. Marshall, Y. Fei, W. Roy Jackson and A. L. Chaffee, *Fuel*, 2023, **337**, 126839.
15 R. Borgohain, J. G. Handique, A. K. Guha and S. Pratihar, *J. Phys. Org. Chem.*, 2018, **31**, e3757.

16 I. Gonul, M. Kose, G. Ceyhan and S. Serin, *Inorg. Chim. Acta*, 2016, **453**, 522–530.
17 K. Sztanke, A. Maziarka, A. Osinka and M. Sztanke, *Bioorg. Med. Chem.*, 2013, **21**, 3648–3666.
18 M. S. Karthikeyan, D. J. Prasad, B. Poojary, K. Subrahmanya Bhat, B. S. Holla and N. S. Kumari, *Bioorg. Med. Chem.*, 2006, **14**, 7482–7489.
19 M. W. Amer, E. M. Khdeir and F. Barzagli, *Energy Fuels*, 2025, **39**, 11147–11158.
20 M. W. Amer, E. M. Khdeir, L. E. Haimour, S. I. Aljariri Alhesan, F. Barzagli and K. A. Alzughoul, *Int. J. Coal Prep. Util.*, 2024, **44**, 665–682.
21 S. Yadamani, A. Neamati, M. Homayouni-Tabrizi, S. A. Beyramabadi, S. Yadamani, A. Gharib, A. Morsali and M. Khashi, *Breast*, 2018, **41**, 107–112.
22 W.-J. Lian, X.-T. Wang, C.-Z. Xie, H. Tian, X.-Q. Song, H.-T. Pan, X. Qiao and J.-Y. Xu, *Dalton Trans.*, 2016, **45**, 9073–9087.
23 A. Zianna, G. D. Geromichalos, A. G. Hatzidimitriou, E. Coutouli-Argyropoulou, M. Lalia-Kantouri and G. Psomas, *J. Inorg. Biochem.*, 2019, **194**, 85–96.
24 D. Aggoun, M. Fernández-García, D. López, B. Bouzerafa, Y. Ouennoughi, F. Setifi and A. Ourari, *Polyhedron*, 2020, **187**, 114640.
25 S. N. Mbugua, N. R. S. Sibuyi, L. W. Njenga, R. A. Odhiambo, S. O. Wandiga, M. Meyer, R. A. Lalancette and M. O. Onani, *ACS Omega*, 2020, **5**, 14942–14954.
26 I. Waziri, T. L. Yusuf, E. Akintemi, M. T. Kelani and A. Muller, *J. Mol. Struct.*, 2023, **1273**, 134382.
27 G. P. Oliveira, M. A. Lima, G. B. S. Pereira, A. R. Costa, A. A. Batista, M. R. Forim, M. R. Cominetti, R. D. Zanetti, R. L. Farias, A. V. G. Netto, J. H. Araujo-Neto, J. A. Ellena, L. Olmedo-Moreno, V. Capilla-Gonzalez and F. V. Rocha, *J. Mol. Struct.*, 2025, **1322**, 140306.
28 M. Jiang, X. Su, X. Zhong, Y. Lan, F. Yang, Y. Qin and C. Jiang, *J. Mol. Struct.*, 2024, **1318**, 139403.
29 E. Basaran, H. Gamze Sogukomerogullari, R. Cakmak, S. Akkoc, T. Taskin-Tok and A. Köse, *Bioorg. Chem.*, 2022, **129**, 106176.
30 R. Ouyang, S. Wang, K. Feng, C. Liu, D. Z. Silva, Y. Chen, Y. Zhao, B. Liu, Y. Miao and S. Zhou, *J. Inorg. Biochem.*, 2023, **244**, 112205.
31 A. Palanimurugan and A. Kulandaisamy, *J. Organomet. Chem.*, 2018, **861**, 263–274.
32 L. H. Abdel-Rahman, A. M. Abu-Dief, H. Moustafa and S. K. Hamdan, *Appl. Organomet. Chem.*, 2017, **31**, e3555.
33 S. Bashir, S. R. Maqsood, G. M. Peerzada, B. Khan and M. A. Rizvi, *J. Inorg. Chem.*, 2014, **2014**, 1–11.
34 Z. Faghih, A. Neshat, A. Wojtczak, Z. Faghih, Z. Mohammadi and S. Varestan, *Inorg. Chim. Acta*, 2018, **471**, 404–412.
35 N. C. Campanella, M. D. S. Demartini, C. Torres, E. T. D. Almeida and C. M. C. P. Gouvêa, *Genet. Mol. Biol.*, 2012, **35**, 159–163.
36 S. Chandra, S. Gautam, H. K. Rajor and R. Bhatia, *Spectrochim. Acta, Part A*, 2015, **137**, 749–760.
37 F. Trudu, F. Amato, P. Vaňhara, T. Pivetta, E. M. Peña-Méndez and J. Havel, *J. Appl. Biomed.*, 2015, **13**, 79–103.
38 A. R. Kapdi and I. J. S. Fairlamb, *Chem. Soc. Rev.*, 2014, **43**, 4751–4777.
39 M. D. Coskun, F. Ari, A. Y. Oral, M. Sarimahmut, H. M. Kutlu, V. T. Yilmaz and E. Ulukaya, *Bioorg. Med. Chem.*, 2013, **21**, 4698–4705.
40 A. C. F. Caires, E. T. Almeida, A. E. Mauro, J. P. Hemerly and S. R. Valentini, *Quim. Nova*, 1999, **22**, 329–334.
41 N. Cutillas, G. S. Yellol, C. De Haro, C. Vicente, V. Rodríguez and J. Ruiz, *Coord. Chem. Rev.*, 2013, **257**, 2784–2797.
42 E. Ulukaya, F. Ari, K. Dimas, E. I. Ikitimur, E. Guney and V. T. Yilmaz, *Eur. J. Med. Chem.*, 2011, **46**, 4957–4963.
43 E. Z. Jahromi, A. Divsalar, A. A. Saboury, S. Khaleghizadeh, H. Mansouri-Torshizi and I. Kostova, *J. Iran. Chem. Soc.*, 2016, **13**, 967–989.
44 P. L. Holland, *Acc. Chem. Res.*, 2008, **41**, 905–914.
45 L. Kakaliou, B. Qian, S. W. Baek, M. R. Smith and D. H. Motry, *Inorg. Chem.*, 1999, **38**, 5964–5977.
46 D.-P. Song, X.-C. Shi, Y.-X. Wang, J.-X. Yang and Y.-S. Li, *Organometallics*, 2012, **31**, 966–975.
47 S. J. Lucas, R. M. Lord, R. L. Wilson, R. M. Phillips, V. Sridharan and P. C. McGowan, *Dalton Trans.*, 2012, **41**, 13800.
48 R. M. Lord, A. J. Hebden, C. M. Pask, I. R. Henderson, S. J. Allison, S. L. Shepherd, R. M. Phillips and P. C. McGowan, *J. Med. Chem.*, 2015, **58**, 4940–4953.
49 R. M. Lord, M. Zegke, I. R. Henderson, C. M. Pask, H. J. Shepherd and P. C. McGowan, *Chem.–Eur. J.*, 2019, **25**, 495–500.
50 C. R. Madzivire, P. Caramés-Méndez, C. M. Pask, R. M. Phillips, R. M. Lord and P. C. McGowan, *Inorg. Chim. Acta*, 2019, **498**, 119025.
51 S. H. Van Rijt, A. J. Hebden, T. Amaresekera, R. J. Deeth, G. J. Clarkson, S. Parsons, P. C. McGowan and P. J. Sadler, *J. Med. Chem.*, 2009, **52**, 7753–7764.
52 K. D. Camm, A. El-Sokkary, A. L. Gott, P. G. Stockley, T. Belyaeva and P. C. McGowan, *Dalton Trans.*, 2009, 10914.
53 D. Taher, N. H. Al-Said, M. Albanna, M. Kloda, M. Mustafa, W. Helal, K. I. Assaf, W. Hourani, W.-R. Kotob, S. Saleh, A. Makahleh and M. M. Rabba'a, *Inorg. Chim. Acta*, 2025, **583**, 122711.
54 D. Taher, S. Saleh, A. Y. Habashneh, W. Hourani, M. Mustafa, W. Helal, M. Al-Noaimi, S. M. Obeidat, M. Kloda, T. Alhindi, M. H. Kailani and A. Ghazzy, *J. Mol. Struct.*, 2025, **1340**, 142542.
55 A. S. Abushamleh, K. A. Abu-Safieh, M. A. Khanfar, D. Taher, L. Tahtamouni and N. J. Alwahsh, *J. Struct. Chem.*, 2021, **62**, 1112–1122.
56 K. Döring, D. Taher, B. Walfort, M. Lutz, A. L. Spek, G. P. M. Van Klink, G. Van Koten and H. Lang, *Inorg. Chim. Acta*, 2008, **361**, 2731–2739.
57 D. Taher, B. Walfort and H. Lang, *Inorg. Chim. Acta*, 2006, **359**, 1899–1906.
58 D. Taher, B. Walfort, G. Van Koten and H. Lang, *Inorg. Chem. Commun.*, 2006, **9**, 955–958.

59 D. Taher, B. Walfort and H. Lang, *Inorg. Chem. Commun.*, 2004, **7**, 1006–1009.
60 H. Lang, K. Döring, D. Taher, U. Siegert, B. Walfort, T. Rüffer and R. Holze, *J. Organomet. Chem.*, 2009, **694**, 27–35.
61 H. Lang, D. Taher, B. Walfort and H. Pritzkow, *J. Organomet. Chem.*, 2006, **691**, 3834–3845.
62 D. Taher, J. R. Wilson, G. Ritch, M. Zeller and N. K. Szymczak, *Chem. Commun.*, 2021, **57**, 5718–5721.
63 G. K. Anderson, M. Lin, A. Sen and E. Gretz, in *Inorganic Syntheses*, ed. R. J. Angelici, John Wiley & Sons, Inc., Hoboken, NJ, USA, 2007, pp. 60–63.
64 H. Gielen-Haertwig, V. Min, J.-M. Li, U. Rosentreter, K.-H. Schlemmer, S. Allerheiligen, L. Telan, L. Bärfacker, J. Keldenich, M. F. Fitzgerald, K. Nash, B. Albrecht and D. Meurer, Dihydropyridine derivatives for use as human neutrophil elastase inhibitors, *WO Pat.*, WO2004020412A1, 2004.
65 D. M. Granum, P. J. Riedel, J. A. Crawford, T. K. Mahle, C. M. Wyss, A. K. Begej, N. Arulsamy, B. S. Pierce and M. P. Mehn, *Dalton Trans.*, 2011, **40**, 5881.
66 I. Hilker, J. F. G. A. Jansen and W. Posthumus, Thermosetting resin composition, *WO Pat.*, WO2014076072A1, 2014.
67 M. Kidwai, S. Bhardwaj, N. K. Mishra, V. Bansal, A. Kumar and S. Mozumdar, *Catal. Commun.*, 2009, **10**, 1514–1517.
68 O. Marvi and L. Z. Fekri, *CCHTS*, 2018, **21**, 19–25.
69 H. Neelakantan, H.-Y. Wang, V. Vance, J. D. Hommel, S. F. McHardy and S. J. Watowich, *J. Med. Chem.*, 2017, **60**, 5015–5028.
70 G. Xie, Y. Li, J. Sun and C. Qian, *Inorg. Chem. Commun.*, 2009, **12**, 796–799.
71 G. Xie, W. Song, T. Li, X. Xu, Z. Lan, Y. Li and A. Zhang, *J. Appl. Polym. Sci.*, 2014, **131**, DOI: 10.1002/app.41178.
72 D. Zheglova, D. Genov, S. Bolvig, P. Hansen, M. Hanfland and E. Dooryhee, *Acta Chem. Scand.*, 1997, **51**, 1016–1023.
73 E. Yoshida and S. Yamada, *Bull. Chem. Soc. Jpn.*, 1965, **38**, 2179–2182.
74 A. N. Nesmeyanov, O. V. Nogina and V. A. Dubovitskii, *Russ. Chem. Bull.*, 1968, **17**, 514–520.
75 Z. Ishtaiwi, D. Taher, M. Korb, W. Helal, H. K. Juwhari, A. Al-Hunaiti, H. Amarne, K. Assaf, L. Alrawashdeh, M. W. Amer, Y. A. Yousef and H. Lang, *J. Mol. Struct.*, 2023, **1288**, 135747.
76 Z. Ishtaiwi, D. Taher, M. Korb, W. Helal, A. Al-Hunaiti, H. K. Juwhari, H. Amarne, M. W. Amer, Y. A. YouSef, S. Klaib and S. T. Abu-Orabi, *Arabian J. Chem.*, 2022, **15**, 104349.
77 D. Taher, F. F. Awwadi, M. Al-Noaimi, L. K. Khader, H. K. Juwhari, H. Amarne, M. H. Kailani and A. Ibdah, *Inorg. Chim. Acta*, 2019, **487**, 409–418.
78 D. Taher, F. F. Awwadi, J. M. Speck, M. Korb, D. Schaarschmidt, S. Weheabby, A. Y. Habashneh, M. Al-Noaimi, M. El-Khateeb, S. T. Abu-Orabi and H. Lang, *J. Organomet. Chem.*, 2017, **845**, 55–62.
79 D. Taher, F. F. Awwadi, J. M. Speck, M. Korb, C. Wagner, E. M. Hamed, M. Al-Noaimi, A. Y. Habashneh, M. El-khateeb, S. T. Abu-Orabi, K. Merzweiler and H. Lang, *J. Organomet. Chem.*, 2017, **847**, 59–67.
80 D. Taher, F. F. Awwadi, J. M. Speck, M. Korb, D. Schaarschmidt, C. Wagner, H. Amarne, K. Merzweiler, G. Van Koten and H. Lang, *J. Organomet. Chem.*, 2018, **863**, 1–9.
81 H. Kargar, M. Fallah-Mehrjardi, R. Behjatmanesh-Ardakani, M. Bahadori, M. Moghadam, M. Ashfaq, K. S. Munawar and M. N. Tahir, *Polyhedron*, 2022, **213**, 115622.
82 D. Taher, S. Klaib, M. Korb, K. I. Assaf, G. Rheinwald and H. Lang, *J. Mol. Struct.*, 2024, **1312**, 138510.
83 H. Amarne, W. Helal, D. Taher, M. Korb and A. Al-Hunaiti, *Mol. Cryst. Liq. Cryst.*, 2022, **743**, 77–88.
84 R. M. Al-As'ad, K. A. Khalyfeh, D. Taher, K. I. Assaf, M. H. Tawara, T. Rüffer and H. Lang, *J. Organomet. Chem.*, 2024, **1013**, 123170.
85 M. A. Spackman and D. Jayatilaka, *CrystEngComm*, 2009, **11**, 19–32.
86 R. Tiwari and M. Nath, *New J. Chem.*, 2015, **39**, 5500–5506.
87 M. M. Ibrahim, A. M. Fathy, S. A. Al-Harbi, S. A. Sallam, S. S. Al-Juaid and A. E.-M. M. Ramadan, *J. Organomet. Chem.*, 2021, **939**, 121764.
88 Ö. Şahin, Ü. Ö. Özdemir, N. Seferoğlu, Z. K. Genc, K. Kaya, B. Aydıner, S. Tekin and Z. Seferoğlu, *Photobiol*, 2018, **178**, 428–439.
89 V. Nagalakshmi, M. Sathya, M. Premkumar, D. Kaleeswaran, G. Venkatachalam and K. Balasubramani, *J. Organomet. Chem.*, 2020, **914**, 121220.
90 S. Munusamy, P. Muniyappan and V. Galmari, *J. Coord. Chem.*, 2019, **72**, 1910–1921.
91 L. F. Dechouk, A. Bouchoucha, Y. Abdi, K. Si Larbi, A. Bouzaheur and S. Terrachet-Bouaziz, *J. Mol. Struct.*, 2022, **1257**, 132611.
92 M. Krause, R. Von Der Stück, D. Brünink, S. Buss, N. L. Doltsinis, C. A. Strassert and A. Klein, *Inorg. Chim. Acta*, 2021, **518**, 120093.
93 A. N. Gupta, V. Kumar, V. Singh, K. K. Manar, M. G. B. Drew and N. Singh, *CrystEngComm*, 2014, **16**, 9299–9307.
94 L. Zhou, Q. Hu, L.-Q. Chai, K.-H. Mao and H.-S. Zhang, *Polyhedron*, 2019, **158**, 102–116.
95 X. Chen, Q. Zhou, Y. Cheng, Y. Geng, D. Ma, Z. Xie and L. Wang, *J. Lumin.*, 2007, **126**, 81–90.
96 D. Fabra, J. P. Mészáros, A. I. Matesanz, G. Spengler, F. Aguilar Rico, G. Moreno-Alcántar, A. Casini, É. A. Enyedy and A. G. Quiroga, *Inorg. Chem.*, 2025, **64**, 22852–22865.
97 F. Navas, F. Mendes, I. Santos, C. Navarro-Ranninger, S. Cabrera and A. G. Quiroga, *Inorg. Chem.*, 2017, **56**, 6175–6183.
98 Z. Sondka, N. B. Dhir, D. Carvalho-Silva, S. Jupe, K. McLaren, M. Starkey, S. Ward, J. Wilding, M. Ahmed, J. Argasinska, D. Beare, M. S. Chawla, S. Duke, I. Fasanella, A. G. Neogi, S. Haller, B. Hetenyi, L. Hodges, A. Holmes, R. Lyne, T. Maurel, S. Nair, H. Pedro, A. Sangrador-Vegas, H. Schuilenburg, Z. Sheard,

S. Y. Yong and J. Teague, *Nucleic Acids Res.*, 2024, **52**, D1210–D1217.
99 X. Liu, Q. Zhou, J. R. Hart, Y. Xu, S. Yang, D. Yang, P. K. Vogt and M.-W. Wang, *Proc. Natl. Acad. Sci. U. S. A.*, 2022, **119**, e2215621119.
100 E. R. Wood, L. M. Shewchuk, B. Ellis, P. Brignola, R. L. Brashear, T. R. Caferro, S. H. Dickerson, H. D. Dickson, K. H. Donaldson, M. Gaul, R. J. Griffin, A. M. Hassell, B. Keith, R. Mullin, K. G. Petrov, M. J. Reno, D. W. Rusnak, S. M. Tadepalli, J. C. Ulrich, C. D. Wagner, D. E. Vanderwall, A. G. Waterson, J. D. Williams, W. L. White and D. E. Uehling, *Proc. Natl. Acad. Sci. U. S. A.*, 2008, **105**, 2773–2778.
101 C. Nilewski, S. Labadie, B. Wei, S. Malhotra, S. Do, L. Gazzard, L. Liu, C. Shao, J. Murray, Y. Izrayelit, A. Gustafson, N. F. Endres, F. Ma, X. Ye, J. Zou and M. Evangelista, *ACS Med. Chem. Lett.*, 2024, **15**, 21–28.
102 L. Buckbinder, D. J. St. Jean, T. Tieu, B. Ladd, B. Hilbert, W. Wang, J. T. Alltucker, S. Manimala, G. V. Kryukov, N. Brooijmans, G. Dowdell, P. Jonsson, M. Huff, A. Guzman-Perez, E. L. Jackson, M. D. Goncalves and D. D. Stuart, *Cancer Discovery*, 2023, **13**, 2432–2447.
103 K. Stakyte, M. Rotheneder, K. Lammens, J. D. Bartho, U. Grädler, T. Fuchß, U. Pehl, A. Alt, E. Van De Logt and K. P. Hopfner, *Nat. Struct. Mol. Biol.*, 2021, **28**, 789–798.
104 S. J. Isakoff, J. A. Engelman, H. Y. Irie, J. Luo, S. M. Brachmann, R. V. Pearline, L. C. Cantley and J. S. Brugge, *Cancer Res.*, 2005, **65**, 10992–11000.
105 H. Hu, J. Zhu, Y. Zhong, R. Geng, Y. Ji, Q. Guan, C. Hong, Y. Wei, N. Min, A. Qi, Y. Zhang and X. Li, *Ann. Transl. Med.*, 2021, **9**, 410.
106 T. Junttila, *Trends Cardiovasc. Med.*, 2000, **10**, 304–310.
107 Y. Pylayeva-Gupta, E. Grabocka and D. Bar-Sagi, *Nat. Rev. Cancer*, 2011, **11**, 761–774.
108 A. D. Cox, S. W. Fesik, A. C. Kimmelman, J. Luo and C. J. Der, *Nat. Rev. Drug Discovery*, 2014, **13**, 828–851.
109 I. A. Prior, F. E. Hood and J. L. Hartley, *Cancer Res.*, 2020, **80**, 2969–2974.
110 Y. Shiloh and Y. Ziv, *Nat. Rev. Mol. Cell Biol.*, 2013, **14**, 197–210.
111 P. A. Jeggo and M. Löbrich, *Biochem. J.*, 2015, **471**, 1–11.
112 D. A. Fruman, H. Chiu, B. D. Hopkins, S. Bagrodia, L. C. Cantley and R. T. Abraham, *Cell*, 2017, **170**, 605–635.
113 S. Sunoqrot, S. Abusulieh and O. H. Abusara, *Int. J. Pharm.*, 2023, **645**, 123392.
114 O. Alkhaldi, S. Abusulieh, O. H. Abusara and S. Sunoqrot, *Int. J. Pharm.*, 2024, **665**, 124674.
115 CCDC 2478443: Experimental Crystal Structure Determination, 2026, DOI: 10.5517/ccdc.csd.cc2p60sq.